Proceedings of the 2007 IEEE/RSJ International
Conference on Intelligent Robots and Systems
San Diego, CA, USA, Oct 29 - Nov 2, 2007

Dynamics of Step-climbing with Deformable Wheels and Applications for Mobile Robotics

Alexander Wilhelm, William Melek, *Sr. Member, IEEE*, Jan Huissoon, Chris Clark,
Gerd Hirzinger, Norbert Sporer, Matthias Fuchs

***Abstract*—Wheeled-mobile robots operating in human environments typically encounter small steps. Surmounting steps is normally not considered when determining peak torque needs, yet it can be the maximum requirement. This work looks at the statics and dynamics of this situation to determine the necessary peak torque. It finds that using a dynamic model that includes the wheel elasticity is essential for properly representing a real-world tire. When torque is increased using a step function, energy is stored in the tire—higher tire elasticity eases climbing. Knowledge of this phenomenon could facilitate the use of smaller actuators. The model is numerically integrated and results are found to agree with experiment.**

I. Introduction

DETERMINING the torque requirements for powered wheeled vehicles is typically based on acceleration and velocity requirements, e.g. [1], [2]. However, for vehicles that must surmount small steps at slow speeds, e.g. indoor mobile robots, climbing the step can easily be the peak torque demand. A simple static analysis of this situation using rigid elements is insufficient to explain the behavior of a deformable wheel typically used in indoor mobile robotics, and overestimates the required torque. Some tire models designed for car tires can handle steps [3], [4], but these cannot be easily translated to typical robot tires and their complexity makes it difficult to understand the underlying phenomenon in passing over steps. In this paper, an easy to use dynamic model that includes wheel elasticity is developed to properly describe step-passing behavior.

The remainder of this paper is organized as follows: in II.A, a simple static model is developed. This model is extended in II.B into a dynamic model, and is non-dimensionalized in order to allow comparison of different designs. A simulation is performed in III, and results are compared to experiment in IV. Finally, the implications of the model results are discussed in V and conclusions about the improved model are drawn in VI.

Manuscript received April 9, 2007.

A. N. Wilhelm is with the University of Waterloo, Waterloo, N2L 3G1 Canada (e-mail: anwilhel@engmail.uwaterloo.ca).

J. Huissoon is with the University of Waterloo (e-mail: jph@uwaterloo.ca).

W. Melek is with the University of Waterloo (e-mail: wmelek@mecheng1.uwaterloo.ca).

C. Clark is with California Polytechnic State University, San Luis Obispo, CA 93407 (e-mail: cmclark@calpoly.edu).

G. Hirzinger is with the German Aerospace Center (DLR) Institute of Robotics and Mechatronics, D-82230 Weßling, Germany (e-mail: Gerd.Hirzinger@dlr.de)

N. Sporer is with the German Aerospace Center (DLR) Institute of Robotics and Mechatronics, (e-mail: Norbert.Sporer@dlr.de)

M. Fuchs is with the German Aerospace Center (DLR) Institute of Robotics and Mechatronics, (e-mail: Matthias.Fuchs@dlr.de)

II. Theory

A. Rigid-Wheel Model

To create the simple rigid-element model (Fig. 1), the front wheel of radius r is replaced by a rigid link (CF) pin-jointed at one end to the ground and to the cart at the other. The rear wheel is replaced by a pin joint attached to a slider joint at R. It is assumed that the vehicle is front-wheel driven and that the wheels are aligned perpendicular to the step with a radius larger than the step height. The model must be modified to include rear-wheel drive.

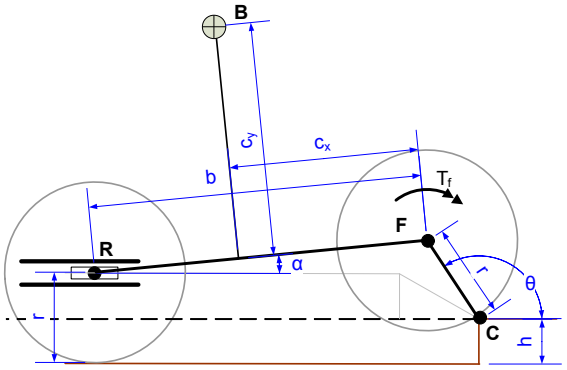

Fig. 1. Rigid system model showing similarities to a slider-crank

Described in this way, the problem is similar to a slider-crank, a mechanism that is often used as an example in literature, e.g. [5], where the front wheel is like the crank. There are several differences from the typical representation of a slider-crank as a device to convert linear into rotational motion: the slider is vertically offset from the crank origin by distance e; the 'connecting rod' (RF) of length b (the vehicle) has a large mass m and inertia I_{CM} at B which is a distance c_x and c_y from F; and, most importantly, the torque T_f is applied not at the 'crank origin' C but at the front wheel centre F. Introducing a torque in the middle of the mechanism means that its reaction also plays a role, acting both on α, the angle of the platform from horizontal, and θ, the angle of CF from horizontal. The mass and inertia of the wheels are neglected.

The maximum torque T_{max} required for static balance of this mechanism occurs at the base of the step and is

$$T_{\max} = \frac{1}{2}\frac{-mgbr\cos\theta_{init}}{b - r\cos\theta_{init}} \qquad (1)$$

when $c_x = b/2$. The cosine of the starting angle θ_{init} can be found as follows:

$$\cos\theta_{init} = -\sqrt{h(2r-h)}/r \,. \tag{2}$$

Combining (1) and (2) using three non-dimensionalized (ND) groups, $T_{\max}/mgb$, b/r, h/r, results in the ND expression for maximum torque

$$\frac{T_{\max}}{mgb} = \frac{1}{2}\left(\sqrt{\frac{h}{r}\left(2-\frac{h}{r}\right)}\Big/\left(\frac{b}{r}+\sqrt{\frac{h}{r}\left(2-\frac{h}{r}\right)}\right)\right) \tag{3}$$

which allows for the observation of generalized trends that hold true for the more detailed model to follow and which are visible in Fig. 2:

- ND peak torque decreases with increasing wheelbase, though the benefits are minimal for large wheelbase-to-wheel-radius ratios (*b/r*). Compared to applying a torque at the origin *C* as in a typical slider-crank, $b/(b+r\cos\theta_{init})$ less peak torque is required.
- A larger wheel radius increases ND peak torque (the moment arm is larger), though the effect is reduced for small step heights.
- ND peak torque increases with step height.

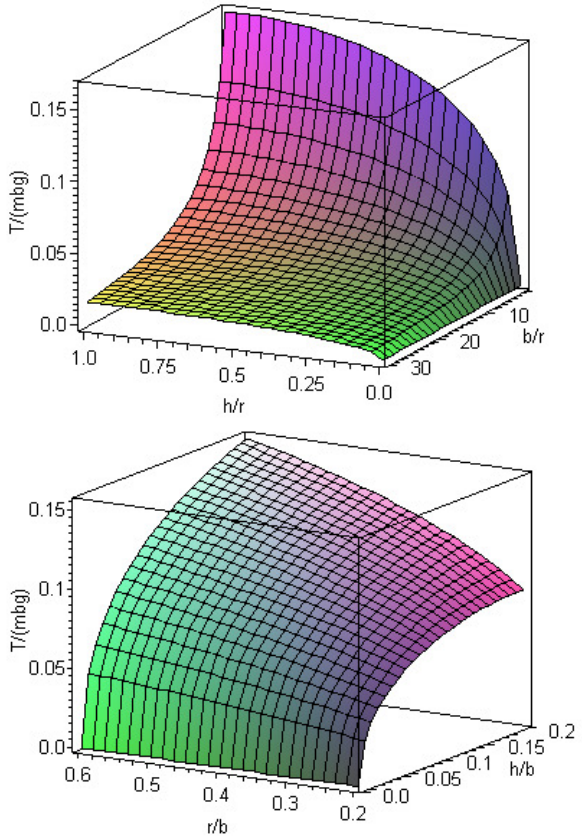

Fig. 2. Static torque relationship for non-dimensionalized parameters.

An important additional consideration is that the friction between the corner and the wheel must be sufficient to prevent slip. Experiments show that the effective friction factor is higher at the corner than on a flat surface, in some cases even exceeding 1—this suggests that there are other forces at play in the indented part of the tire. Nevertheless, the available normal force decreases with increasing *h/r*, reaching zero when *h=r*, at which point a front-wheel-driven platform has reached its ultimate step height limit.

B. *Spring-Damper Wheel Model*

It has been found that modifying the model above in the following way better describes the non-linear dynamics of small-step passing: the rigid 'crank' (*FC*) is replaced with an ideal spring-damper element with spring constant k_c, damping constant k_d and displacement *c*. Also, it is essential to include a ground support force at the base of the tire. This is realized by a vertical spring-damper with spring constant k_v, damping constant k_d, and displacement *d* which only acts when in contact with the ground.

Two different spring constants are used to reflect the fact that the tire behaves differently when compressed on a level surface versus compression on a corner. Tire spring forces become non-linear for large deformations such as at corners, but this simplification has proven effective. The model will lose validity towards the top of the step, where the compression point reverts from a corner to a flat surface and the tire's standard spring constant for level surfaces should begin to apply again. However, this region does not play a role in determining peak torque requirements, since, as is evident from (1), torque required decreases towards zero as cosine θ approaches 90°.

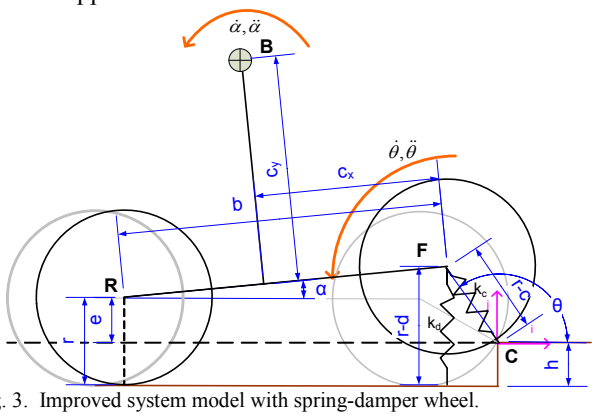

Fig. 3. Improved system model with spring-damper wheel.

With the tire in contact with the ground, the kinetic energy of the system, *T,* can be expressed as

$$T = \tfrac{1}{2}m_b\left(v_b{}^2\hat{i} + v_b{}^2\hat{j}\right) + \tfrac{1}{2}I_{cm}\dot{\alpha}^2 \tag{4}$$

where m_b is the system mass, I_{cm} the system inertia expressed at B, and v_b, the velocity of B, is

$$\begin{aligned} v_b\hat{i} &= c_x\dot{\alpha}\sin\alpha - c_y\dot{\alpha}\cos\alpha - \dot{c}\cos\theta - R\dot{\theta}\sin\theta \\ v_b\hat{j} &= -c_x\dot{\alpha}\cos\alpha - c_y\dot{\alpha}\sin\alpha - \dot{c}\sin\theta + R\dot{\theta}\cos\theta \end{aligned} \tag{5}$$

where *R* is the effective radius,

$$R = r - c \tag{6}$$

and the potential energy, *U*, can be expressed as

$$U = \frac{1}{2}k_c c^2 + \frac{1}{2}k_d d^2 + m_b g\left(R\sin\theta - c_x\sin\alpha + c_y\cos\alpha\right) \tag{7}$$

where time derivatives are expressed in dot notation.

To express the motion of the system using Lagrange's

equations, four generalized coordinates, α, θ, c, d are chosen and are related by the constraint equations

$$C_1 = \lambda_1\left(b\sin\alpha - R\sin\theta + e\right) \tag{8}$$

$$C_2 = \lambda_2\left(e - d - R\sin\theta\right) \tag{9}$$

that relate α to θ and d to c & θ respectively, where λ_1, λ_2 are Lagrange multipliers and where

$$e = r - h\,. \tag{10}$$

The Lagrangian L is

$$L = T - U - C_1 - C_2\,. \tag{11}$$

External forces are expressed in the generalized coordinates as

$$Q_\alpha = T_f \tag{12}$$

$$Q_\theta = -T_f \tag{13}$$

$$Q_c = k_d\dot{c} \tag{14}$$

$$Q_d = k_d\dot{d}\,. \tag{15}$$

The four dynamic equations are thus found using

$$\frac{d}{dt}\left(\frac{\partial L}{\partial \dot{q}}\right) - \left(\frac{\partial L}{\partial q}\right) = Q_q \tag{16}$$

where q stands for the generalized coordinates α, θ, c, d :

$$d: k_v d - \lambda_2 = -k_v d \tag{17}$$

$$\theta: m_b\begin{pmatrix}\left(c_x\dot{c}\dot{\alpha} - Rc_x\ddot{\alpha}\right)\cos(\chi) + 4R\dot{c}\dot{\theta} + 2R^2\ddot{\theta}\\ +R\dot{\alpha}\left(c_x\sin(\chi)\mathrm{X} + c_y\cos(\gamma)\mathrm{H}\right) + \left(Rc_y\ddot{\alpha} - c_y\dot{c}\dot{\alpha}\right)\sin(\gamma)\\ -\left(c_x\dot{c}\dot{\alpha} + Rc_y\dot{\alpha}\dot{\theta}\right)\cos(\gamma) + \left(c_y\dot{c}\dot{\alpha} - Rc_x\dot{\alpha}\dot{\theta}\right)\sin(\chi)\end{pmatrix}$$
$$+ m_b g\left(R\cos\theta\right) - \lambda_1 R\cos\theta - \lambda_2 R\cos\theta = -T_f \tag{18}$$

$$\alpha: m_b\begin{pmatrix}2\ddot{\alpha}\left(c_y{}^2 + c_x{}^2\right) + \left(c_x\ddot{c} - \dot{c}c_y\dot{\theta} + Rc_y\ddot{\theta}\right)\sin(\gamma)\\ +\left(c_x\dot{c} + Rc_y\dot{\theta}\right)\cos(\gamma)\mathrm{H} + \left(\dot{c}c_x\dot{\theta} + c_y\ddot{c} - Rc_x\ddot{\theta}\right)\cos(\chi)\\ +\left(Rc_x\dot{\theta} - c_y\dot{c}\right)\sin(\chi)\mathrm{X} - \left(c_x\dot{c}\dot{\alpha} + Rc_y\dot{\alpha}\dot{\theta}\right)\cos(\gamma)\\ +\left(c_y\dot{c}\dot{\alpha} - Rc_x\dot{\alpha}\dot{\theta}\right)\sin(\chi)\end{pmatrix}$$
$$+ I_{cm}\ddot{\alpha} + m_b g\left(-c_x\cos\alpha - c_y\sin\alpha\right) + \lambda_1 b\cos\alpha = T \tag{19}$$

$$c: m_b\begin{pmatrix}\left(c_x\ddot{\alpha} + c_y\dot{\alpha}\dot{\theta}\right)\sin(\gamma) + c_x\dot{\alpha}\cos(\gamma)\mathrm{H} + 2\ddot{c}\\ +\left(c_y\ddot{\alpha} - c_x\dot{\alpha}\dot{\theta}\right)\cos(\chi) - c_y\dot{\alpha}\sin(\chi)\mathrm{X} - 2R\dot{\theta}^2\end{pmatrix} \tag{20}$$
$$+ k_c c - m_b g\sin\theta + \lambda_1\sin\theta + \lambda_2\sin\theta = -k_d$$

and the following substitutions are made to conserve space:

$$\chi = \theta + \alpha \tag{21}$$

$$\gamma = \theta - \alpha \tag{22}$$

$$\mathrm{X} = \dot{\theta} + \dot{\alpha} \tag{23}$$

$$\mathrm{H} = \dot{\theta} - \dot{\alpha} \tag{24}$$

d can be eliminated by substituting the constraint relationship and its derivative,

$$d = -R\sin\theta + e \tag{25}$$

$$\dot{d} = \dot{c}\sin\theta - R\dot{\theta}\cos\theta \tag{26}$$

into (17), which we can then be solved for λ_2:

$$\lambda_2 = \left(\dot{c} - R\right)k_v\sin\theta + ek_v - Rk_v\dot{\theta}\cos\theta\,. \tag{27}$$

Eliminating the Lagrange multipliers at this point is preferable to including them in the numerical integration [6]. Solving for λ_1 using (19) and substituting λ_1, λ_2 into (18) and (20) gives (38) and (39) found in Appendix A that are time-dependent functions of $\ddot{\alpha}, \dot{\alpha}, \alpha, \ddot{\theta}, \dot{\theta}, \theta, \ddot{c}, \dot{c}, c$ only.

Similarly, α can be eliminated using

$$\sin\alpha = \left(R\sin\theta + e\right)/b \tag{28}$$

$$\cos\alpha = \sqrt{b^2 - \left(-R\sin\theta + e\right)^2}\,/b \tag{29}$$

$$\dot{\alpha} = \left(-\dot{c}\sin\theta + R\dot{\theta}\cos\theta\right)/\left(b\cos\alpha\right) \tag{30}$$

$$\ddot{\alpha} = \frac{\begin{pmatrix}r\ddot{\theta}\cos\theta - r\dot{\theta}^2\sin\theta - \ddot{c}\sin\theta + \dot{c}^2\cos\theta\\ -\dot{c}\dot{\theta}\cos\theta - c\ddot{\theta}\cos\theta + c\dot{\theta}^2\sin\theta + \dot{\alpha}^2 b\sin\alpha\end{pmatrix}}{b\cos\alpha}\,. \tag{31}$$

We are left with two equations that can be rearranged into the form

$$\ddot{\theta} = f\left(\dot{\theta}, \theta, \dot{c}, c\right) \tag{32}$$

$$\ddot{c} = f\left(\dot{\theta}, \theta, \dot{c}, c\right) \tag{33}$$

which can then be integrated numerically. Integration must be stopped when $d > 0$ and the final coordinates used as initial conditions for the system equations without ground contact that are described below.

To model the dynamics when the tire is not touching the ground, the potential energy and damping force of the ground contact spring-damper is set to zero, eliminating the external work Q_d and making the new potential energy term

$$U_{offground} = \tfrac{1}{2}k_c c^2 + m_b g\left(R\sin\theta - c_x\sin\alpha + c_y\cos\alpha\right) \tag{34}$$

Only three generalized coordinates α, θ, c and one constraint equation, (6), are now needed, which are solved as before. Numerical integration is performed until $d < 0$, at which point the first set of dynamic equations must be used, and the process repeated *ad infinitum*.

In order to easily compare different mobile platforms, the equations and results can be non-dimensionalized with the following 18 ND groups:

$$\frac{c_x}{b}, \frac{c_y}{b}, \frac{h}{r}, \frac{b}{r}, \frac{T}{mgb}, k_c\frac{b}{mg}, k_v\frac{b}{mg}, k_d\frac{b^{3/2}}{m\sqrt{g}}, \frac{I_{CM}}{mb^2},$$
$$\theta, \dot{\theta}\sqrt{\frac{b}{g}}, \ddot{\theta}\frac{b}{g}, \frac{c}{r}, \frac{\dot{c}}{\sqrt{gb}}, \frac{\ddot{c}}{g}, \frac{d}{r}, \frac{\dot{d}}{\sqrt{gb}}, \frac{\ddot{d}}{g}$$

To determine what friction factor, μ_c, is necessary at the corner to prevent slip, one must determine the radial normal force,

$$F_N = k_c c + k_d\dot{c} \tag{35}$$

and the tangential force,

$$F_T = T_f\,/R\,. \tag{36}$$

The friction factor to prevent slippage is

$$\mu_c = F_T/F_N\,. \tag{37}$$

Note that there is an additional friction force at the ground contact point so long as $d < 0$, during which time the above

TABLE II
EXPERIMENTAL & SIMULATION RESULTS

Step Height (mm)	Theoretical Static Torque[a] (Nm)	Torque Input Type	Experimental Torque	% difference to static torque	Simulation Torque	% difference to experimental torque
8.42	3.53±0.29	step	2.67±0.05	-24	2.67	0.0
		ramp	3.23±0.13		3.19	
16.00	4.63±0.43	step	3.89±0.06	-16	3.91	0.3
		ramp	5.07±0.17		4.44	-12

[a] based on the wheel radius as measured on a flat surface

equations do not apply.

Since $\underline{\mu_c}$ fluctuates somewhat due to the changes in tire compression c, for a corner with a particular friction factor there will be a set of parameters creating a border-line case where some slippage occurs during tire compression. However, periods of traction while the tire is less compressed are sufficient such that the wheel will still surmount the step. Determining this point would require extending the model to include slip.

Other possible extensions include consideration of non-powered wheels, where the external force comes from a different point, and of rear wheels, which are loaded more heavily because platform tilt moves the CM towards the back, thus causing them to need more torque. Also, approaching the step with a velocity or acceleration lowers the torque requirements but can lead to undesired oscillations and lift-off after impact.

III. SIMULATION

A. Setup

The vertical spring constant was determined experimentally, as no published data was available for the tire. The radial spring constant was found by calibrating the model to fit the experimental data. The model will be poor for step heights much greater than those used during calibration. For example, for no step, the radial spring constant should be the same as the tire's normal spring constant for flat ground. Thus, calibration should be performed to include the expected maximum step height to ensure the model is accurate when finding the peak torque required for this height. A damping value for both dampers of 200 N·m/s was chosen; results were found to have low sensitivity to changes in damping within a range (50–500) typical for tires.

TABLE I
EXPERIMENTAL CART SPECIFICATIONS

Component	Details
Drive Motor	Maxon RE 40 – 148877 DC Brush, 150W, 48V Rated 0.148 Nm @ 7000 rpm, Peak 2.5 Nm
Drive Gearing	15:1 - Maxon GP 42C – 203116, 2 Stage 2:1 Toothed Pulley Efficiency: 79% max at rated torque
Drive Wheel	IMPAC 32-86 IS300 foam filled, polyamide surface 6" x 1 ¼" (152.4 mm x 31.75 mm) nominal, 147.6 mm x 31 mm measured undeformed, 100 mm hub diameter
Wheelbase	0.477m
Cart Mass	20.64 kg
Cart Inertia[a] ($kg \cdot m^2$)	I_{xx}:0.929, I_{xy}:-0.256, I_{xz}:0.001, II_{yy}:1.24, I_{yz}:0.007, I_{zz}:1.959, relative to CM, where x is forward, z is up
Cart CM	0.25m above tire centre, 0.215m behind tire centre

The simulation was created using the Modelica language and its multi-body physics library [7], which is implemented in Dymola [8], allowing for animation and easy programming of loss-of-contact conditions. It was run using the 'Dassl' integrator set to a tolerance of 1e-5. Results were compared to direct numerical integration of the dynamic equations from section II in Maple using the Runge-Kutta Fehlberg method [9] and found to be identical. Parameters for wheelbase, mass, inertia, centre of mass, wheel radius and step height were chosen to match the experimental setup (Table I). Note that the 3D functionality of the library was made use of to include the cart's off-diagonal inertia terms in order to improve agreement with experiment.

The torque input T_f was varied for each simulation run until the minimum value sufficient to overcome the step was found.

Adding a vertical spring-damper element to simulate the rear tire, including gear-train dynamics, including gear-train elasticity and backlash, and adding motor dynamics all had negligible impact.

B. Analysis

Because the elastic tire compresses, the effective wheel radius is reduced. The small reduction due to compression, on the order of 3% with the parameters used in the simulation, causes a 1.7% reduction in torque in the static analysis. However, the reduction in radius is not the only benefit of an elastic tire.

From Fig. 5 - Fig. 4 that show results for the 16 mm step, it is apparent that the elastic tire first absorbs energy in the radial spring element while the cart is still partially supported by the ground. The spring compresses, spring potential energy increases, and it only slowly starts contributing to the total vertical support force. The vertical ground contact spring expands, releasing stored energy as its component of the vertical support force diminishes until it vanishes completely when ground contact is lost at 3.07 seconds. The radial spring then continues damped oscillations, contributing a vertical force component that puts the vertical force on average at the same level as the rigid system – this despite a lower torque and thus a lower contribution from the torque reaction to the vertical force.

Since the system is nearly conservative with small loses due to damping, the elasticity only acts to redistribute the energy over time, but this is sufficient to reduce the peak torque.

IV. EXPERIMENT

A. Setup

A three-wheeled cart with one driven wheel (Fig. 8) was

used in experiments, details of which are given in table I. Torque was controlled using a Copley Controls 4122CE run in torque mode, where a reference and monitor signal are set and recorded by a PC-based controller/DAQ at 10kHz. Controller reaction times were found to be significantly smaller than observed physical behavior.

Two different step heights – 8.42 mm and 16 mm or 11% and 22% of undeformed tire radius, representing 84% and 105% of rated motor torque for static balance – were tested. The tire was a modified polyurethane foam-filled wheelchair tire of type IMPAC 32-86 IS300 with a polyamide surface and nominal dimensions of 6" x 1 ¼ ".

An initial torque of 0.73 Nm was applied to eliminate play in the system and bring the wheel into contact with the corner.

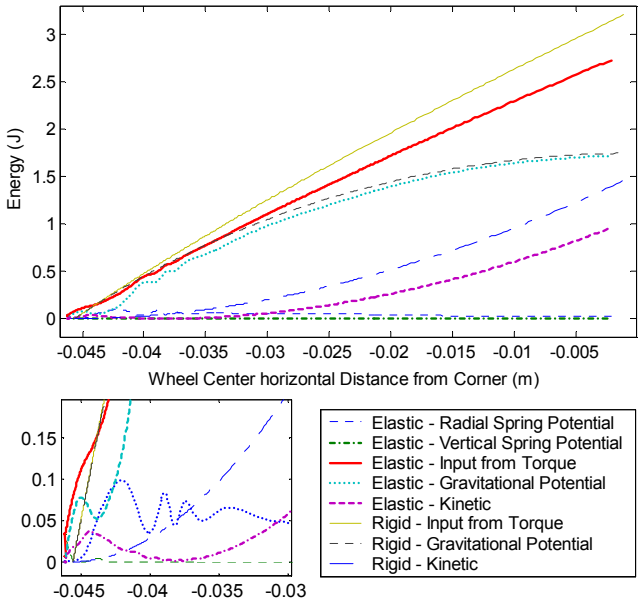

Fig. 4. Energy for 16 mm step height, comparing rigid and elastic tire

B. Results

Slowly increasing current (and thus torque) to achieve a near static condition—increasing torque in small increments and waiting for motor rotation to settle—causes the platform to pass over the step within range of the calculated static value. Increasing the current from 0.73 Nm to the test value in one step requires a smaller value to pass over the step, which agrees with the model presented in section II.B. The results are compared in table II; the theoretical static torque value is calculated from equation (1), where uncertainty is propagated from the measurement uncertainty in the physical variables (r, h, m, c_x, c_y, b). Experimental results for both step heights agree well with simulation. This also shows the effective spring constant to be applicable at least over this range. A video comparing experimental and simulation results for a 16 mm step trial with torque increase by step-function is provided, both clearly showing similar oscillations due to tire elasticity. The slight movement of the step occurred because its supports were removed to facilitate camera placement for filming.

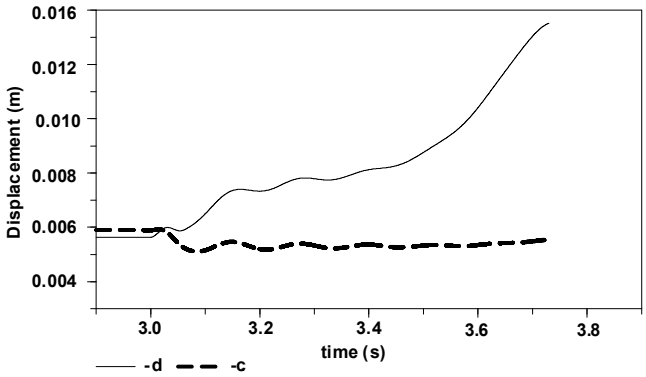

Fig. 5. Spring compression, 16 mm step height, torque step from 0.73 to 3.91Nm at 3 s, tire lifts off ground at 3.07 s.

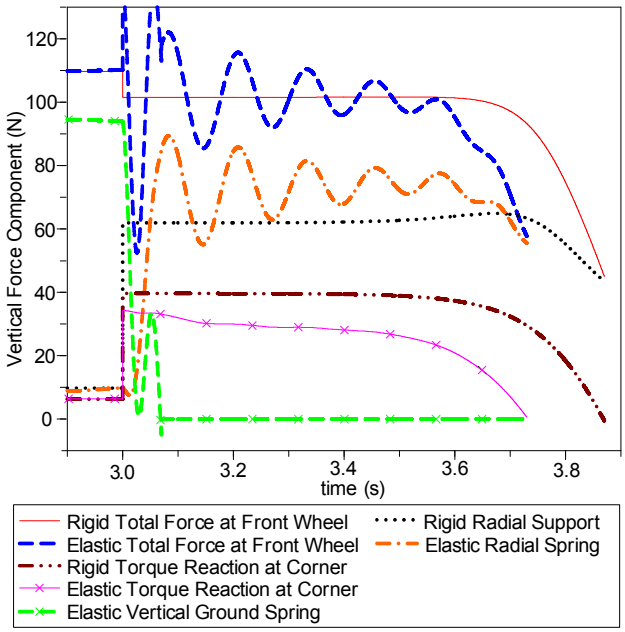

Fig. 6. Forces at front wheel resolved into vertical components for both spring-damper and rigid model, 16 mm step height. Torque step from 0.73 to 3.91 Nm at 3 s for elastic wheel, 0.73 to 4.63 Nm for rigid wheel. Elastic wheel reaches top of step at 3.66 s, rigid wheel at 3.86 s.

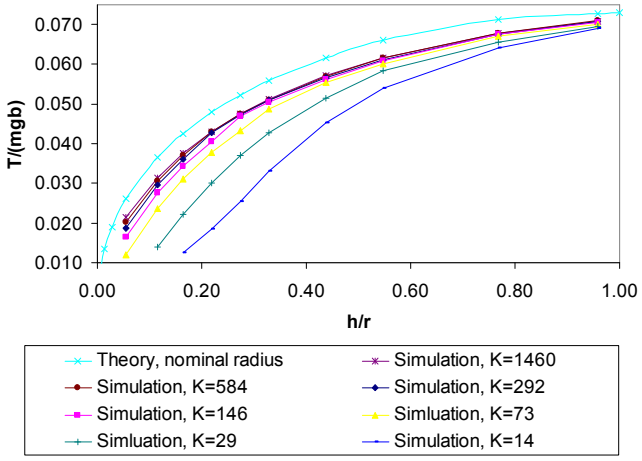

Fig. 7. ND static torque compared to simulation results showing effect of different ND spring constants, where $K = k_c\, b/mg$ and all other ND groups are held at experimental conditions. K=146 is experimental setup.

V. Parametric Analysis of Dynamic Response

From Fig. 7 a number of observations can be made. The reduction in ND peak torque with the elastic tire, both in relative and absolute terms, is largest at small step-height-to-radi us ratios and with soft spring constants. It gets relatively smaller quickly as the step height to radius ratio increases, and also decreases in absolute terms, though this decrease is at a fairly low rate, particularly for hard spring constants. At high *h/r* ratios, the curves converge, approaching but not reaching the static curve.

In general, a softer spring increases the time period over which energy can be stored and released, reducing the peak torque required. Its ability to do so appears dependent on the *h/r* ratio (likely because of the initial contact angle, θ_{init}). Of course, a softer tire may have unwanted repercussions in the vehicle's overall behavior, where high stiffness is often desirable for instance to improve positioning accuracy of a mounted sensor or end-effector. Thus, the benefits of a large soft tire for step passing must be weighed against potential negatives for each application.

A larger wheel can climb higher steps because its initial contact angle θ is higher, increasing the radial normal force and thus decreasing the necessary friction factor. However, it requires more torque, takes up more space, weighs more, and tends to have a higher rolling resistance.

VI. Conclusions

The dynamic model of step-climbing presented in section II.B is much better at predicting the necessary torque to overcome the step than a static rigid model. It accurately demonstrates the reduced torque required due to energy storage in an elastic tire, as is evident from the agreement between experimental and model results. Using the ND parameters, different mobile robot designs can be evaluated and compared for their step-climbing ability. Since climbing small steps is a significant torque requirement, especially when approached at slow speed, and potentially the highest torque requirement in some mobile robotics applications, modeling this situation more accurately will lead to lower actuator requirements with associated benefits for mass and power consumption. It will also allow for better selection of tire characteristics—choosing between suspension and step–passing qualities.

Fig. 8. Cart used for experiments.

VII. Appendix A

$$
\begin{aligned}
&m_b\begin{pmatrix}(c_x\dot{c}\dot{\alpha}-Rc_x\ddot{\alpha})\cos(\chi)+(Rc_y\ddot{\alpha}-c_y\dot{c}\dot{\alpha})\sin(\gamma)\\ +R\dot{\alpha}(c_x\sin(\chi)\mathrm{X}+c_y\cos(\gamma)\mathrm{H})\\ +4R\dot{c}\dot{\theta}+2R^2\ddot{\theta}-(c_x\dot{c}\dot{\alpha}+Rc_y\dot{\alpha}\dot{\theta})\cos(\gamma)\\ +(c_y\dot{c}\dot{\alpha}-Rc_x\dot{\alpha}\dot{\theta})\sin(\chi)\end{pmatrix}b\cos\alpha+\\
&m_b\begin{pmatrix}2\ddot{\alpha}(c_y{}^2+c_x{}^2)+(c_x\ddot{c}-\dot{c}c_y\dot{\theta}+Rc_y\ddot{\theta})\sin(\gamma)\\ +(c_x\dot{c}+Rc_y\dot{\theta})\cos(\gamma)\mathrm{H}+(c_y\dot{c}\dot{\alpha}-Rc_x\dot{\alpha}\dot{\theta})\sin(\chi)\\ +(\dot{c}c_x\dot{\theta}+c_y\ddot{c}-Rc_x\ddot{\theta})\cos(\chi)\\ +(Rc_x\dot{\theta}-c_y\dot{c})\sin(\chi)\mathrm{X}-(c_x\dot{c}\dot{\alpha}+Rc_y\dot{\alpha}\dot{\theta})\cos(\gamma)\end{pmatrix}R\cos\theta\\
&+m_bgR\cos\theta(b\cos\alpha-c_x\cos\alpha-c_y\sin\alpha)\\
&+I_{cm}\ddot{\alpha}R\cos\theta+T_f(b\cos\alpha-R\cos\theta)\\
&-((\dot{c}-R)k_v\sin\theta+ek_v-Rk_v\dot{\theta}\cos\theta)Rb\cos\theta\cos\alpha=0
\end{aligned}
\tag{38}
$$

$$
\begin{aligned}
&m_b\begin{pmatrix}(c_x\ddot{\alpha}+c_y\dot{\alpha}\dot{\theta})\sin(\gamma)+k_cc+k_d+(\dot{c}-R)k_vb\sin^2\theta\\ +ek_vb\sin\theta+(c_y\ddot{\alpha}-c_x\dot{\alpha}\dot{\theta})\cos(\chi)-c_y\dot{\alpha}\sin(\chi)\mathrm{X}\\ +2\ddot{c}-2R\dot{\theta}^2-Rk_vb\dot{\theta}\cos\theta\sin\theta+c_x\dot{\alpha}\cos(\gamma)\mathrm{H}\end{pmatrix}b\cos\alpha\\
&-m_b\begin{pmatrix}2\ddot{\alpha}(c_y{}^2+c_x{}^2)+(c_x\ddot{c}-\dot{c}c_y\dot{\theta}+Rc_y\ddot{\theta})\sin(\gamma)\\ +(c_x\dot{c}+Rc_y\dot{\theta})\cos(\gamma)\mathrm{H}+(c_y\dot{c}\dot{\alpha}-Rc_x\dot{\alpha}\dot{\theta})\sin(\chi)\\ +(\dot{c}c_x\dot{\theta}+c_y\ddot{c}-Rc_x\ddot{\theta})\cos(\chi)\\ +(Rc_x\dot{\theta}-c_y\dot{c})\sin(\chi)\mathrm{X}-(c_x\dot{c}\dot{\alpha}+Rc_y\dot{\alpha}\dot{\theta})\cos\gamma\\ g(c_x\cos\alpha+c_y\sin\alpha-b\cos\alpha)\end{pmatrix}\sin\theta\\
&-I_{cm}\ddot{\alpha}\sin\theta+T_f\sin\theta=0
\end{aligned}
\tag{39}
$$

References

[1] R. Holmberg and O. Khatib, "Development and control of a holonomic mobile Robot for mobile manipulation Tasks," *Int. J. Robotics Research*, vol 19; pp. 1066-1074, Nov. 2000.

[2] T. B. Park, J. H. Lee,) B.-J.Yi, W. K. Kim, B. J. You, S.-R. Oh, "Optimal design and Actuator sizing of redundantly actuated omni-directional mobile Robots," Proc. IEEE Int. Conf. Robotics & Automation, May 2002.

[3] M. Gipser, "ADAMS/FTire - A Tire Model for ride & durability Simulations." Available: http://www.ftire.com./download/ftire_eng_2.pdf

[4] P.W.A. Zegelaar and H.B. Pacejka, "The In-plane Dynamics of Tyres on uneven Roads" *Vehicle System Dynamics*, 25 (Suppl.), pp. 714–730, 1996.

[5] J.-L. Ha, R.-F. Fung, K.-Y. Chen, and S.-C. Hsien, "Dynamic modeling and identification of a slider-crank Mechanism," *J. Sound a. Vibration*, vol. 289, pp. 1019–1044, 2006.

[6] R. E. Ellis and S. L. Ricker, "Two numerical Issues in simulating constrained Robot Dynamics," *IEEE Trans. Systems, Man, a.Cybernetics*, vol. 24, no. 1, pp. 19-27, Jan. 1994.

[7] M. Otter, H. Elmqvist, S.E. Mattsson, "The New Modelica MultiBody Library," in 2003 Proc. Int. Modelica Conf., pp. 311-330.

[8] "Dymola Dynamic Modeling Laboratory," Ver. 6, Dynasim AB, 2006.

[9] "dsolve/numeric/rkf45" *Maple Online Help*, Ver. 10, Waterloo Maple Inc., Waterloo, Canada, 2005.